Published in "Physical Review B - Condensed matter and materials physics
85(21): 214503 , 2012"
which should be cited to refer to this work.

Macroscopic phase segregation in superconducting $K_{0.73}Fe_{1.67}Se_2$ as seen by muon spin rotation and infrared spectroscopy

C. N. Wang,[1] P. Marsik,[1] R. Schuster,[1] A. Dubroka,[1,2] M. Rössle,[1] Ch. Niedermayer,[3] G. D. Varma,[4] A. F. Wang,[5] X. H. Chen,[5] T. Wolf,[6] and C. Bernhard[1]

[1]*Department of Physics and Fribourg Centre for Nanomaterials, University of Fribourg, Chemin du Musée 3, CH-1700 Fribourg, Switzerland*
[2]*Department of Condensed Matter Physics, Faculty of Science, Masaryk University, Kotlářská 2, CZ-61137 Brno, Czech Republic and Central European Institute of Technology, Kotlářská 2, CZ-61137 Brno, Czech Republic*
[3]*Laboratory for Neutron Scattering, Paul Scherrer Institut, CH-5232 Villigen, Switzerland*
[4]*Department of Physics, Indian Institute of Technology Roorkee, Roorkee 247667, India*
[5]*Department of Physics, Hefei National Laboratory for Physical Sciences at Microscale, University of Science and Technology of China, Hefei, Anhui 230026, China*
[6]*Karlsruhe Institut für Technologie, Institut für Festkörperphysik, D-76021 Karlsruhe, Germany*

Using muon spin rotation and infrared spectroscopy, we investigated the recently discovered superconductor $K_{0.73}Fe_{1.67}Se_2$ with $T_c \approx 32$ K. We show that the combined data can be consistently described in terms of a macroscopically phase-segregated state with a matrix of ∼88% volume fraction that is insulating and strongly magnetic and inclusions with an ∼12% volume fraction, which are metallic, superconducting, and nonmagnetic. The electronic properties of the latter, in terms of the normal state plasma frequency and the superconducting condensate density, appear to be similar as in other iron selenide or arsenide superconductors.

The recent discovery of superconductivity with T_c above 30 K in the alkali-metal intercalated iron chalcogenide with the nominal composition $K_{0.8}Fe_{2-y}Se_2$[1,2] has led to great efforts to better understand their unusual electronic and magnetic properties.[3] Superconductivity is reported to occur here in the presence of a very strong antiferromagnetic order with a Néel temperature of $T_N \approx 560$ K and a large magnetic moment of $\sim 3.6 \mu_B$ per Fe ion.[4] Meanwhile, it is well established that high-temperature superconductivity in the cuprates[5–7] and iron arsenides[8–11] occurs in close proximity to an antiferromagnetic state. Nevertheless, the static magnetic order is usually strongly suppressed or even entirely absent in the superconducting part of the phase diagram. Another unusual feature concerns the extremely low electronic conductivity of these iron selenide superconductors.[12,13] It implies that the concentration of itinerant charge carriers is more than an order of magnitude smaller than in their cuprate and iron arsenide counterparts where it is already considered to be very low. This has led to speculations that the mechanism of superconductivity in these chalcogenides may be different and even more unconventional than in the cuprate and iron arsenide high-temperature superconductors. Alternatively, there exists mounting evidence that this material may be spatially inhomogeneous consisting of a matrix that is strongly antiferromagnetic and insulating and inclusions that are metallic and superconducting.[14–18] Since a coherent superconducting response is observed in electric transport and macroscopic magnetization measurements,[2] the latter phase must either amount to a significant volume fraction or else its inclusions must be specifically shaped and arranged such that percolation is achieved along certain pathways.

In the following, we present a combined muon-spin-rotation (μSR) and infrared spectroscopy study, which supports a macroscopic phase-segregation scenario. In good agreement with recent reports,[14,17,18] our μSR data establish the presence of two phases that are either strongly magnetic or entirely nonmagnetic and superconducting with volume fractions of ∼88% and ∼12%, respectively. They yield an estimate of the magnetic penetration depth of $\lambda_{ab} \approx 270$ nm that is similar as in the other iron arsenide, selenide, or cuprate superconductors with corresponding T_c values.[12,13,19,20] We also show that, by adopting the volume fractions as obtained from μSR, a reasonable description of the infrared spectra can be obtained with an effective medium approximation (EMA). The model uses an insulating matrix and metallic inclusions for which the Drude response has a similar plasma frequency as in other iron selenide or arsenide superconductors. The shape of the metallic inclusions appears to be elongated such that percolation is achieved despite the low volume fraction.

Superconducting single crystals with a composition of $K_{0.73}Fe_{1.67}Se_2$ (KFS_SC) were grown in Hefei, China as described in Refs. 2 and 21. Corresponding nonsuperconducting and insulating crystals with a nominal composition $K_{0.75}Fe_{1.60}Se_2$ (KFS_I) were prepared in Karlsruhe, Germany. They were grown from K (3N5), Fe (3N), and Se (6N) at a ratio of 0.75:1.6:2 in a vertical Bridgman setup. The starting mixture was filled into a tipped Al_2O_3 crucible that was sealed in a steel container before the crystal growth was carried out in a tubular furnace by cooling from 1050 °C to 770 °C at a rate of 0.4 °C/h. Electric transport measurements confirmed the weakly metallic and superconducting properties of KFS_SC with a superconducting transition at $T_c \approx 32$ K as shown in Fig. 1.

The μSR measurements were performed on crystals with an area of about 5 mm^2 using the GPS setup at the πM3 beamline of the Paul Scherrer Institut in Villigen, Switzerland, which provides a beam of 100% spin-polarized muons. μSR measures the time evolution of the spin polarization $P(t)$ of the implanted muon ensemble via the time-resolved asymmetry of the muon decay positrons.[22] The technique is well suited to

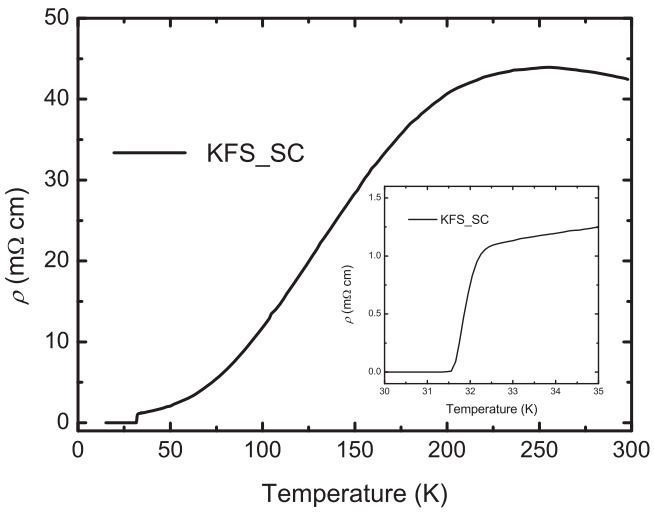

FIG. 1. Temperature dependence of the in-plane resistivity of a KFS_SC single crystal from the same growth batch as the samples used for the μSR and infrared measurements.

studies of magnetic and superconducting materials as it allows a microscopic determination of the internal field distribution and can give direct access to the volume fractions of the superconducting and magnetic phases. The positive muons are implanted into the bulk of the sample and stop at well-defined interstitial lattice sites.[23] The muon ensemble is distributed in a layer of 100–200-μm thickness and, therefore, probes a representative part of the sample volume. Each muon spin precesses in the local magnetic field B_μ with a precession frequency of $\nu_\mu = \gamma_\mu B_\mu/2\pi$ where $\gamma_\mu = 2\pi \times 135.5$ MHz T^{-1} is the gyromagnetic ratio of the muon.

The infrared spectroscopy was performed on freshly cleaved surfaces of the same crystals that were used for the μSR study. Details of the IR ellipsometry and reflection techniques and the analysis of the combined data are described in Refs. 24–26. Special care was taken to avoid any degradation of the surface due to the contact with the ambient. The samples were mounted in an argon gas atmosphere using a glove box and were quickly inserted into the cryostat of the ellipsometer, which then was immediately evacuated. For the IR reflectivity measurements, the crystals were even *in situ* cleaved inside the cryostat at a temperature of about 5 K. Corresponding reflectivity measurements on crystals that were *ex situ* cleaved before mounting them in the cryostat confirmed that the weak electronic response of the superconducting crystals as shown in the following does not originate from a degraded surface but is instead an intrinsic property of the bulk of these samples.

Figure 2 summarizes our transverse-field (TF) μSR experiments on samples KFS_SC and KFS_I at an external magnetic field $H_{ext} = 0.1$ kOe that was applied parallel to the c axis of the crystals. Figure 2(a) shows the muon spin polarization $P(t)/P(t = 0)$ for KFS_SC at 38 K just above $T_c = 32$ K. The major part of the signal exhibits an extremely rapid depolarization that is not even captured within the experimental resolution of 0.625 ns. The remaining part is oscillatory and relaxes only very slowly. The fast relaxing component was previously reported for superconducting crystals with a nominal composition of $Cs_{0.8}Fe_2Se_2$ (Ref. 27) and was interpreted in terms of the antiferromagnetic order of the large Fe moments. The observation of two components with such drastically different relaxation rates is suggestive of an inhomogeneous state, which consists of spatially separated regions that are either strongly magnetic or nonmagnetic. The amplitudes of the very fast and the slowly relaxing parts of the μSR signal of about 15% and 85% can be directly related to the volume fractions of these phases. In doing so, one only has to consider that 2% to 3% of the slowly depolarizing μSR signal arises from muons that stop outside the sample in the sample holder or the cryostat walls. We, thus, arrive at a volume fraction of ~88% for the strongly magnetic phase and ~12% for the nonmagnetic one. The latter is most likely superconducting, whereas, the former remains insulating as shown below based on the infrared data. Notably, very similar volume fractions have been very recently reported in Ref. 28. Our interpretation is also confirmed by the corresponding data on the nonsuperconducting sample KFS_I as shown in Fig. 2(c). Here, only 2% to 3% of the signal due to the background muons remains slowly relaxing, whereas, the entire signal from the muons stopping in the sample is now rapidly depolarized.

The alternative explanation of the TF-μSR data in terms of two different muon stopping sites in the unit cell seems rather unlikely. It would require a second muon site where the local magnetic field vanishes despite the very large Fe moments. Furthermore, since the nonmagnetic signal occurs only for the superconducting crystals, the presence of this highly symmetric muon site would have to be linked to the appearance of a metallic and superconducting state.

Our interpretation that the slowly relaxing component arises from a certain fraction of the sample volume that is nonmagnetic and superconducting is supported by the temperature dependence of the muon spin relaxation rate. As shown in Figs. 2(b) and 2(d), it exhibits a pronounced increase below $T_c = 32$ K that is characteristic of the formation of a superconducting vortex lattice. As shown by the solid lines in Fig. 2, the TF-μSR data were analyzed with the following function:

$$P(t) = P(0)\Big[A_f \cos(\gamma_\mu B_{\mu,f} t + \varphi)\exp(-\lambda_f t) + A_s \cos(\gamma_\mu B_{\mu,s} t + \varphi)\exp\left(-\frac{\sigma_s^2 t^2}{2}\right)\Big]. \quad (1)$$

Here, A_f and A_s are the amplitudes of the fast and slowly relaxing components, respectively, γ_μ is the gyromagnetic ratio of the muon, B_μ is the local magnetic field at the muon site, λ_f is the exponential relaxation rate of the fast component, φ is the initial phase of the muon spins, and σ_s is the Gaussian relaxation rate of the slowly relaxing component. In the normal state, the small and T-independent value of σ_s is determined by the nuclear magnetic moments. The order parameter like, increase of σ_s below T_c signifies the formation of a superconducting vortex lattice. Assuming that the size of the superconducting inclusions is large enough to enable the formation of a regular vortex lattice in their interior, we derive, from the low-temperature value of $\sigma_s \approx 1.35\ \mu s^{-1}$, an estimate of the in-plane magnetic penetration depth of $\lambda_{ab} \approx 270$ nm. Notably, this value of λ_{ab} agrees well with the one reported in Ref. 28, and it is similar as in other iron arsenide[11,29–31] and cuprate superconductors with a comparable T_c value.[19,32]

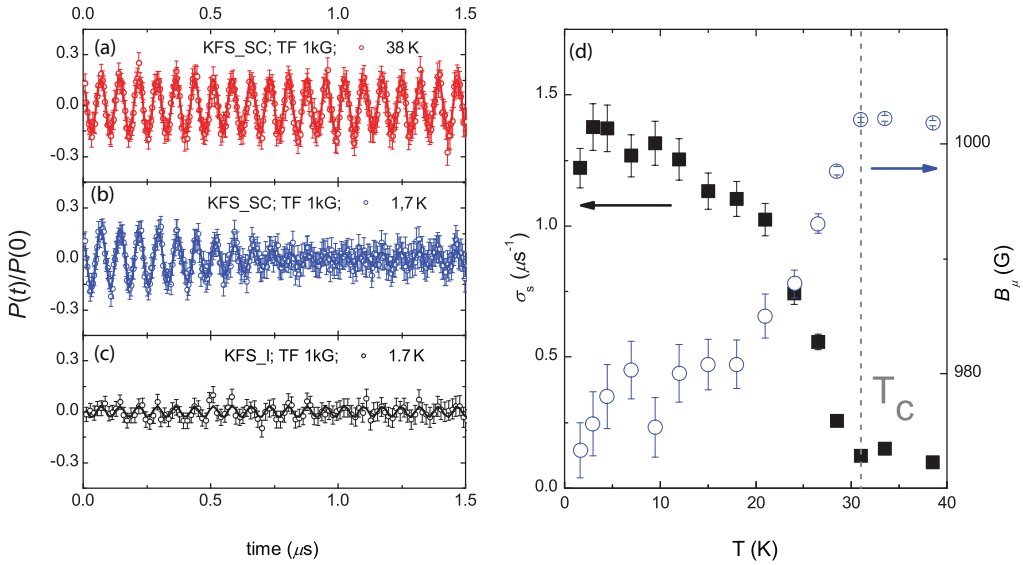

FIG. 2. (Color online) Representative TF-μSR data (symbols) of (a) and (b) KFS_SC just above and below $T_c \approx 32$ K, respectively, and (c) of KFS_I. Solid lines show the fits obtained with the function in Eq. (1). (d) Temperature dependence of the local field B_μ and the relaxation rate σ_s of the slowly relaxing signal of sample KFS_SC.

The superconducting origin of the enhanced relaxation below T_c has been furthermore established with a so-called pinning experiment, which reveals the presence of a strongly pinned superconducting vortex lattice. Figure 3 displays so-called μSR line shapes that were obtained from a fast-Fourier transformation of the TF-μSR time spectra. The open symbols show the μSR line shape as measured after the sample was cooled to 1.6 K in an applied magnetic field of $H_{appl} = 750$ Oe. It has the expected characteristic shape with a very narrow peak at H_{appl} that arises from the background muons that stop outside the sample and a broader main peak that is shifted to lower fields (diamagnetic shift). The somewhat asymmetric shape with a tail toward higher fields originates from the muons that stop near the vortex cores. The second line shape as shown by the solid symbols was obtained after the applied magnetic field was reduced by 100 Oe from 750 to 650 Oe, while the temperature was kept at 1.6 K. Although the narrow peak due to the background muons follows this reduction of H_{appl}, the broader main part of the μSR line shape remains virtually unchanged. This characteristic behavior, which highlights that the magnetic flux density in the sample, remains unchanged is the hallmark of a type-II superconductor with a strongly pinned vortex lattice. It clearly demonstrates that the nonmagnetic regions of KFS_SC become superconducting below $T_c = 32$ K. The observation of a well-developed and strongly pinned vortex lattice is also consistent with the assumption that these superconducting regions are fairly sizable, i.e., larger than the magnetic penetration depth λ_{ab}. Finally, we note that the TF-μSR data do not provide any specific information about the properties of the strongly magnetic fraction. In particular, due to the extremely large relaxation rate, we cannot tell whether or not this fraction is superconducting.

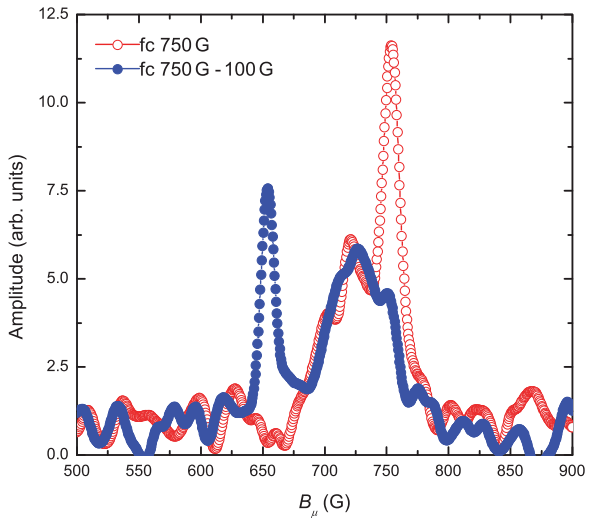

FIG. 3. (Color online) TF-μSR line shapes showing the distribution of local magnetic fields during a so-called pinning experiment as described in the text.

In the following, we present the infrared spectroscopy data, which provide important complementary information about the electronic properties. In particular, we show that they establish that the matrix of KFS_SC is insulating and nonsuperconducting, whereas, the inclusions are metallic with a plasma frequency that is similar as in other iron selenides or arsenides where superconductivity is a bulk phenomenon. Figure 4(a) displays the T dependence of the in-plane reflectivity R_{ab} for KFS_SC in the far-infrared range. As shown by the dotted lines, a Hagen-Rubens relation has been used to extrapolate the data toward zero frequency. We used these reflectivity data in the far infrared together with our ellipsometry data in the mid- and near-infrared ranges to derive a Kramers-Kronig consistent response function. As outlined in Ref. 26, this was obtained by fitting the so-called variational dielectric function, which was composed of a large number of Kramers-Kronig consistent oscillators, to this combined set of spectroscopic data. With the variational dielectric function,

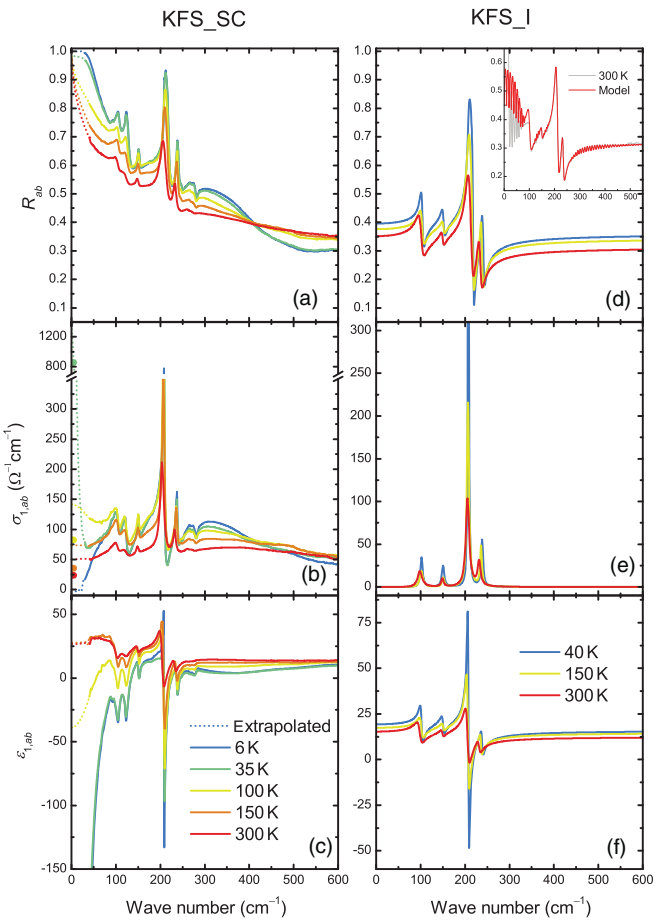

FIG. 4. (Color online) Temperature dependence of the far-infrared spectra of KFS_SC in terms of (a) the in-plane polarized reflectivity R_{ab}, (b) the real part of the optical conductivity $\sigma_{1,ab}$, and (c) the dielectric function $\varepsilon_{1,ab}$. Shown by the circles in (b) is the dc conductivity $\sigma_{\rm dc}$, deduced from the resistivity data in Fig. 1. (d)–(f) Corresponding spectra for KFS_I. Since the crystal was insulating and, thus, transparent, the spectra were corrected for the interference effects that arise from multiple reflections as shown in the inset of (d).

which is intrinsically Kramers-Kronig consistent, we obtained a very good description of the experimental data. The obtained spectra of the real parts of the optical conductivity $\sigma_{1,ab}$ and the dielectric function $\varepsilon_{1,ab}$ are shown in Figs. 4 and 5. Also shown in Fig. 4(b) by the full symbols are the values of the dc conductivity $\sigma_{\rm dc}$ from the resistivity data in Fig. 1. The corresponding values of $\sigma_{1,ab}(\omega \to 0)$ as obtained from the low-frequency extrapolation of our optical data (dotted lines) are consistently somewhat higher. Nevertheless, given the various uncertainties of these transport and optical measurements, the agreement is reasonable, and it validates our low-frequency extrapolation procedure.

In good agreement with previous reports,[13,17,33] we find that these infrared spectra contain only weak signatures of a metallic response. The value of the plasma frequency of the free carriers of $\omega_{\rm pl} \approx 100$–$150$ cm^{-1}, as estimated from the position of the reflection edge in R_{ab} or from an analysis of the optical conductivity with a Drude-Lorentz model, is indeed very small. For a spatially homogeneous sample, it would amount to a free carrier concentration that is about 2 orders of magnitude smaller than in any of the iron selenide/telluride, iron arsenide, or cuprate superconductors.[25,30,34,35] It would also be incompatible with the magnetic penetration depth of $\lambda_{ab} = 270$ nm or a plasma frequency of the superconducting condensate of $\omega_{\rm pl}^{\rm SC} = 5894\,{\rm cm}^{-1}$ as obtained from the μSR data. In addition to the weakly conducting response, the IR spectra exhibit a broad band centered at about 300 cm^{-1}, which is most pronounced at low temperatures. Since this band is much broader than the phonon line shapes, it most likely has an electronic origin.

In the following, we show that this inconsistently weak electronic response and the band at 300 cm^{-1} can be naturally accounted for if one considers that the electronic state may be spatially inhomogeneous. Figure 5 shows that the normal state optical spectra can be very well described in terms of an EMA model. In modeling the spectra, we assumed that the system is composed of an insulating matrix and metallic inclusions with volume fractions of 88% and 12%, respectively, as deduced from the μSR data. The EMA model assumes that the inclusions are randomly oriented ellipsoids with an aspect ratio Q that is treated as a fitting parameter.[36] The dielectric function of the insulating matrix was determined from the optical measurements on sample KFS_I as shown in Figs. 4(d)–4(f). The dielectric function of the conducting inclusions was modeled with two Drude terms, a narrow one to account for the coherent response and a broad one to represent the less coherent background. The fitted plasma frequencies of these Drude peaks, $\omega_{\rm pl,Dn}$ and $\omega_{\rm pl,Db}$, are 3873 and 3162 cm^{-1}, respectively. In addition, we introduced a broad Lorentzian oscillator with a width of 1000 cm^{-1} that is centered at 5000 cm^{-1}.

We found that, in order to reproduce both the very weak free carrier response and the 300 cm^{-1} band, the response has to be modeled as a volume average of two different EMA models, the so-called Maxwell-Garnett (MG) model and the Bruggeman (B) effective medium approximation. The necessity of the combination arises from the well-known properties of the two approaches, i.e., that the MG-EMA describes the resonant plasmonic oscillations occurring in isolated inclusions, which in our model, give rise to the 300 cm^{-1} band, whereas, the low-frequency percolative behavior is reasonably well described by the B-EMA. Specifically, the simulated spectra shown in Fig. 5 were obtained by assuming that percolation is achieved in ~90% of the sample volume (described by the B model), whereas, in ~10%, the metallic inclusions are disconnected by the insulating matrix (accounted for by the MG model). Note that, in both the B- and the MG-EMA models, we used the same volume fraction of the metallic inclusions of 12% as obtained from the μSR experiments. The aspect ratio Q was found to be 0.085 from both MG-EMA and B-EMA models, suggesting that the metallic inclusions have a very elongated needlelike shape. Notably, a similar shape of the inclusions was obtained with an electron backscattering analysis in Ref. 18. In reality, there likely is a variation in the concentration and/or the shape of these metallic inclusions that determines whether percolation is achieved in certain parts of the sample. Nevertheless, we did not allow for such a variation since, as shown below, the presented model describes reasonably well, on a qualitative and even a quantitative level,

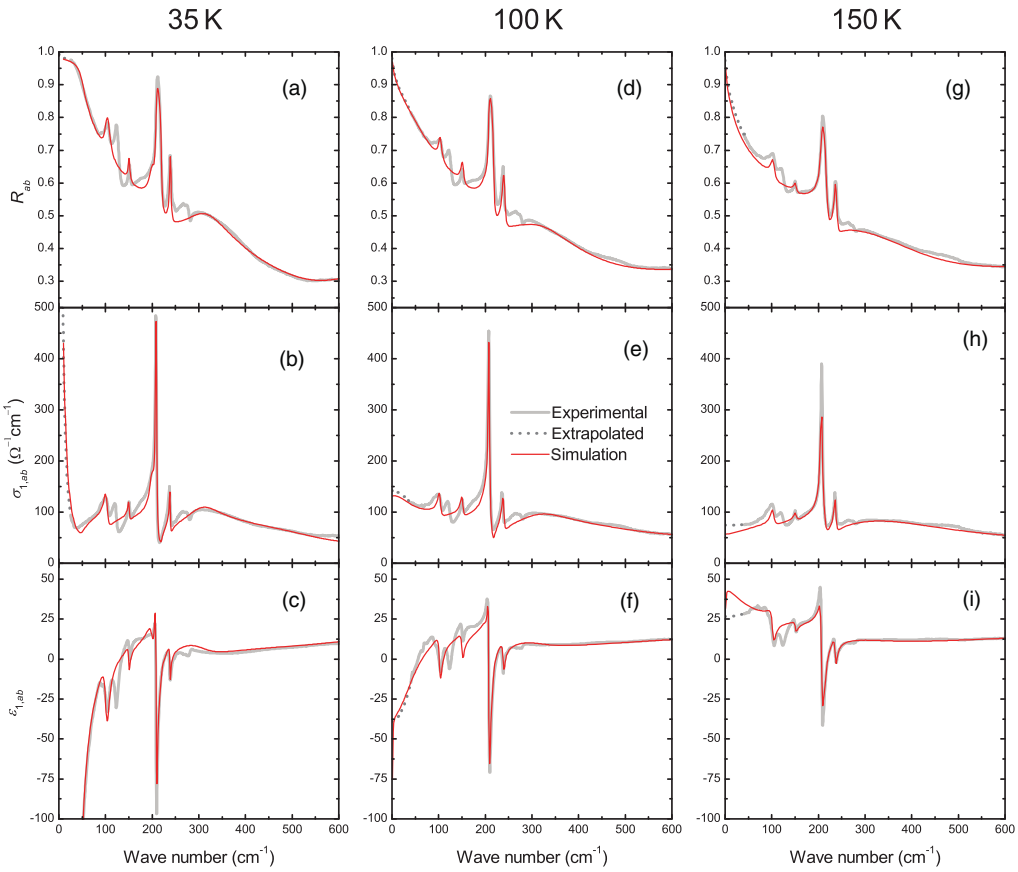

FIG. 5. (Color online) Comparison of the experimental data in the normal state of KFS_SC with the fits based on the EMA model as described in the text.

the key features of the infrared response. Our EMA model also assumes that the inclusions are randomly oriented, whereas, in reality, they may have a preferred direction as indicated in Ref. 37. In this context, we note that our far-infrared ellipsometry data (not shown here), which have been obtained at a grazing angle of incidence (of 80°) yield consistent results for the strength of the electronic mode at 300 cm^{-1} and the weak Drude response as our normal incidence reflection data. This argues against platelike inclusions that are oriented parallel to the sample surface (or the FeSe layers). A more detailed polarization analysis would be required to identify the orientation along {113} planes as reported in Ref. 37.

Effective medium approximations can provide a reasonable description of the optical data as long as the inclusions are much smaller than the wavelength of the radiation inside the sample.[38,39] Since the average value of the index of refraction of our sample is about 4, this gives, for our data in the far-infrared range, wavelengths between 2 and 100 μm. Otherwise, in the limits of inclusion that are larger than the IR wavelength, significant interference and diffraction effects may occur in the optical spectra that are not accounted for by the EMA model. Nevertheless, as shown in Figs. 5 and 8, the EMA model provides a reasonably good description of the experimental data. Based on this reasoning, we estimate that the typical size of these inclusions is less than about 1 μm. This conclusion is similar to the one of a recent electron microscopy paper,[37] revealing a microstructure of $Cs_xFe_{2-y}Se_2$ with plateletlike inclusions that are between 100- and 200 nm thick.

Figure 5 shows that our EMA model enables a reasonable fitting of the normal state spectra. Concerning the electronic response, it accounts well for the small value of the apparent plasma frequency, and it reproduces the broad electronic band around 300 cm^{-1} that becomes pronounced below 100 K. Furthermore, Fig. 5 shows that the B-MG-EMA model accounts for the T dependence in the normal state. The width of the broad Drude peak Γ_{Db} as well as the unscreened plasma frequencies of the narrow and broad Drude peaks $\omega_{\mathrm{pl,Dn}}$ and $\omega_{\mathrm{pl,Db}}$ were fixed at 300, 3873, and 3162 cm^{-1}, respectively. The resulting total unscreened plasma frequency of the two Drude components of $\omega_{\mathrm{pl,D}} \approx 5000$ cm^{-1} is on the same order of magnitude as the one reported for, e.g., bulk iron selenide and arsenide superconductors.[25,40–44] The only parameter that is strongly varied is the width of the narrow Drude peak Γ_{Dn}, whose T dependence is shown in Fig. 6. The very small value of $\Gamma_{\mathrm{Dn}} \approx 5$ cm^{-1} at 35 K just above T_c is a remarkable feature. Although a significantly larger value of about 90 cm^{-1} has been reported for $BaFe_{1-x}Co_xAs_2$,[25] a similarly small value of the scattering rate at low temperatures and low frequencies was obtained for $FeTe_{0.55}Se_{0.45}$ with a so-called extended Drude model analysis.[44] Figure 6 also compares the dc conductivity σ_{dc} as obtained from the resistivity data in Fig. 1 with the low-frequency extrapolated value of $\sigma_{1,ab}(\omega \to 0)$ that is predicted by our EMA model. The values agree reasonably

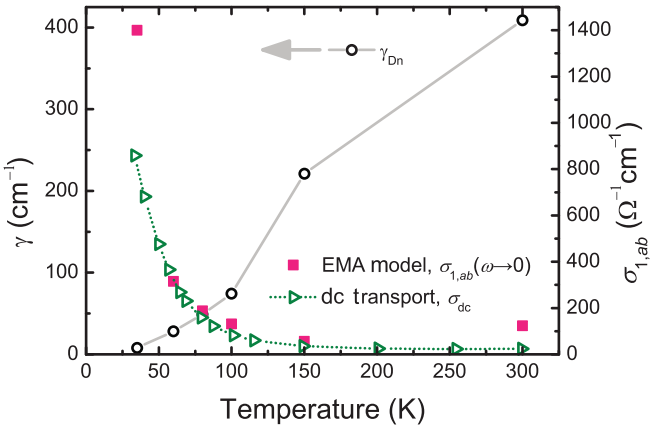

FIG. 6. (Color online) Temperature dependence of the scattering rate of the narrow Drude peak $\Gamma_{\rm Dn} = 1/T_{\rm Dn}$ as obtained from the fitting the with EMA model that is described in the text. Also shown for comparison is the dc conductivity $\sigma_{\rm dc}$, obtained from the resistivity data in Fig. 1 and the extrapolated value of $\sigma_1(\omega \rightarrow 0)$ obtained with the EMA model.

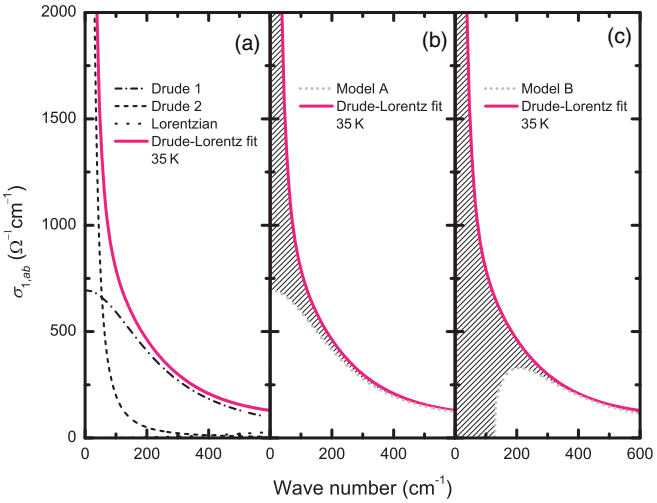

FIG. 7. (Color online) (a) Sketch of the two Drude and the Lorentzian components that were used to fit the data at 35 K just above $T_{\rm c}$. (b) and (c) sketch of the changes due to the onset of superconductivity that were assumed in the context of Model A and Model B, respectively. The shaded area indicates the missing spectral weight that is redistributed toward the origin where it accounts for the response of the superconducting condensate.

well, even at $T = 35$ K where the fit yielded an unusually small scattering rate.

The phonon resonances have not been modeled but are entirely determined by the measured spectra of the insulating sample KFS_I. This approach describes the modes at 104, 150, 210, and 240 cm^{-1}, whereas, it does not account for the ones at 120 and 280 cm^{-1}. This indicates that the metallic inclusions may have a different structure than the insulating matrix. Evidence for an insulating matrix of $K_xFe_4Se_5$ with a $\sqrt{5} \times \sqrt{5}$ Fe-vacancy ordering and superconducting inclusions of a $K_xFe_2Se_2$ phase containing stoichiometric FeSe layers, has indeed been reported from scanning tunneling spectroscopy measurements[45,46] on samples that are from the same growth batch as KFS_SC. Alternatively, the additional phonons may arise from a minor structural difference between the insulating matrix of the KFS_SC sample and the KFS_I sample that was used for the modeling.

Finally, we discuss the changes of the infrared spectra in the superconducting state. As shown in Fig. 4(a), the reflectivity at 6 K as compared to the one at 35 K exhibits a weak yet noticeable increase below ∼100 cm^{-1}, which may be the signature of a superconducting energy gap. The real part of the optical conductivity at low frequency is suppressed here and the corresponding spectral weight is transferred to a zero-frequency δ function that accounts for the loss-free response of the superconducting condensate. The latter also gives rise to an enhancement of the low-frequency inductive response, which shows up as a decrease in the real part of the dielectric function toward negative values. Nevertheless, an unambiguous identification of such a superconducting condensation effect is complicated by the circumstance that a T-dependent increase in the low-frequency reflectivity occurs already in the normal state. As demonstrated above, it was related to the narrowing of the Drude response. Therefore, it is difficult to ascertain which part of the observed changes below $T_{\rm c}$ is caused by superconductivity. In addition, one has to keep in mind that, for this inhomogeneous system, the effective response of the metallic/superconducting phase is strongly modified with respect to the one of a bulk system. For example, a significant part of the spectral weight of the Drude response as well as that of the δ function, due to the superconducting condensate, does not show up at the origin but instead becomes part of the band at 300 cm^{-1}. Based on this EMA modeling, it is, therefore, rather difficult to determine the finer details of the superconductivity-induced changes in the optical response. Nevertheless, as shown in the following, it can still be used to discuss some exemplary cases.

As a first case (Model A), we assumed that the broad Drude peak remains unaffected by the superconducting transition, whereas, all the charge carriers involved in the narrow Drude peak condense and give rise to a δ function at the origin of the conductivity spectrum. The corresponding conductivities at 35 K just above $T_{\rm c}$ and well below $T_{\rm c}$ are shown in Figs. 7(a) and 7(b), respectively. The shaded area in the latter indicates the so-called "missing spectral weight" that is transferred to the δ function at zero frequency and forms the superconducting condensate. The comparison between the fit and the experimental data is shown in Figs. 8(a)–8(c). The obtained values of the superconducting plasma frequency and the magnetic penetration depth are $\omega_{\rm pl,SC} \approx 3873$ cm^{-1} and $\lambda_{ab} \approx 410$ nm, respectively. The former value is about 2.3 times smaller than the one obtained above from the μSR data. Nevertheless, in comparing these values, we remark that the condensate density, as deduced from μSR experiments, is frequently found to be quite a bit larger than the one derived from infrared spectroscopy.[47]

As a second case (Model B), we assumed that both the broad and the narrow Drude components develop an isotropic superconducting gap. The gap magnitude we assumed to be $2\Delta \approx 16$ meV ≈ 130 cm^{-1} as reported from recent angle-resolved photoemission spectroscopy measurements.[4,48–50] The corresponding conductivities at 35 K just above $T_{\rm c}$ and at 6 K well below $T_{\rm c}$ are displayed in Fig. 7(c). Shown by the

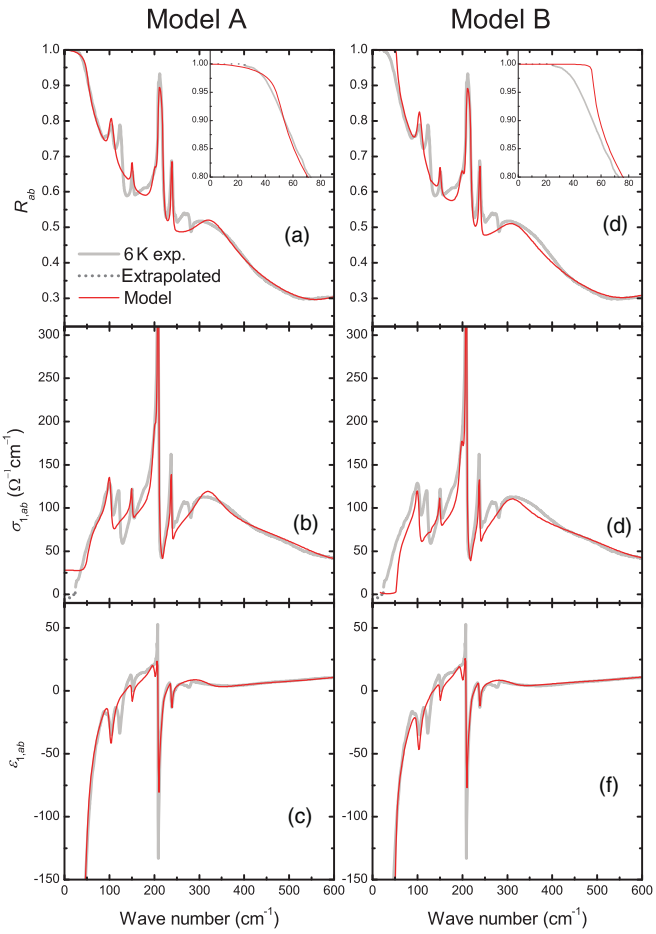

FIG. 8. (Color online) Comparison of the experimental data at 6 K $\ll T_c \approx 32$ K of KFS_SC with the EMA fits using Model A and Model B, respectively. The two models are outlined in the text and are sketched in Figs. 7(b) and 7(c).

shaded area is the missing spectral weight that is transferred to the δ function at zero frequency. The comparison between the fit and the experimental data is shown in Figs. 8(d)–8(f). The isotropic superconducting gap introduces a sharp edge in the reflectivity around 50 cm^{-1} that is not observed in the experimental spectra where the reflectivity rises more gradually toward low frequency and remains below unity in the entire measured range of $\omega > 30$ cm^{-1}. This implies that the low-frequency optical response does not become fully gapped in the superconducting state, i.e., the optical conductivity remains finite as shown in Fig. 8(e). Based on the present data, we cannot answer the question whether this is due to a superconducting gap that is anisotropic in momentum space, a very small or even vanishing gap on one of the conduction bands, or simply some inhomogeneity in the properties of the superconducting inclusions. We note that Model B yields estimates of $\omega_{\mathrm{pl,SC}} \approx 4160$ cm^{-1} and $\lambda_{ab} \approx 380$ nm that are somewhat closer to the μSR values. However, it needs to be remarked that Model B is likely to overestimate the superconducting condensation density. Finally, we note that the sharp reflectivity edge in the modeled spectra occurs at a significantly lower frequency of 50 cm^{-1} than the gap at $2\Delta \approx 130$ cm^{-1} where the reflectivity edge would locate for the case of a homogeneous bulk superconductor. This downward shift in the reflection edge is a consequence of the B-EMA approach; it would not occur if we only used the MG-EMA model.

To summarize, using μSR and infrared spectroscopy, we investigated the magnetic and electronic properties of $K_{0.73}Fe_{1.67}Se_2$ single crystals with $T_c = 32$ K and compared them to the ones of nonsuperconducting crystals with a nominal composition of $K_{0.75}Fe_{1.6}Se_2$. The combined data provide evidence that the superconducting crystals are spatially inhomogeneous with a majority phase (matrix) that is insulating and strongly magnetic and embedded inclusions that are nonmagnetic, metallic, and superconducting. The μSR data established that the latter amount was about 12% of the sample volume. The analysis of the infrared data with a model based on the effective medium approximation revealed that the metallic inclusions have an elongated almost needlelike shape and that percolation between them is achieved in most (but not all) of the sample volume. It also showed that the plasma frequencies of the free carriers as well as of the superconducting condensate density are sizable, e.g., on the same order of magnitude as in other iron selenide and arsenide superconductors.

ACKNOWLEDGMENTS

The work was partially performed at the infrared beamline of the ANKA synchrotron source at KIT Karlsruhe, Germany and at the Swiss muon Source (SμS) at the Paul Scherrer Institut, Villigen, Switzerland. The work at University of Fribourg has been supported by the Swiss National Science Foundation (SNF) Grant No. 200020-129484, by the NCCR MaNEP, and by Project No. 122935 of the Indo-Swiss Joint Research Program. The work at the Central European Institute of Technology was supported by Project No. CZ.1.05/1.1.00/02.0068. The work in Hefei was supported by the Natural Science Foundation of China, the Ministry of Science and Technology of China (973 Project No. 2006CB60100) and the Chinese Academy of Sciences. The work in Germany has been supported by the Deutsche Forschungsgemeinschaft through SPP 1458. R. Schuster appreciates funding through the DFG via Grant No. SCHU/2584/1-1. The financial support from D.S.T. (Government of India) is highly acknowledged.

[1] J. G. Guo, S. F. Jin, G. Wang, S. C. Wang, K. X. Zhu, T. T. Zhou, M. He, and X. L. Chen, Phys. Rev. B **82**, 180520 (2010).
[2] X. G. Luo *et al.*, New J. Phys. **13**, 053011 (2011).
[3] D. X. Mou, L. Zhao, and X. J. Zhou, Front. Phys. **6**, 410 (2011).
[4] W. Bao, Q. Z. Huang, G. F. Chen, M. A. Green, D. M. Wang, J. B. He, and Y. M. Qiu, Chin. Phys. Lett. **28**, 086104 (2011).
[5] C. Niedermayer, C. Bernhard, T. Blasius, A. Golnik, A. Moodenbaugh, and J. I. Budnick, Phys. Rev. Lett. **80**, 3843 (1998).

[6] A. Weidinger, C. Niedermayer, A. Golnik, R. Simon, E. Recknagel, J. I. Budnick, B. Chamberland, and C. Baines, Phys. Rev. Lett. **62**, 102 (1989).
[7] J. H. Brewer *et al*., Phys. Rev. Lett. **60**, 1073 (1988).
[8] C. de la Cruz *et al*., Nature (London) **453**, 899 (2008).
[9] N. Ni, M. E. Tillman, J. Q. Yan, A. Kracher, S. T. Hannahs, S. L. Bud'ko, and P. C. Canfield, Phys. Rev. B **78**, 214515 (2008).
[10] H. H. Klauss *et al*., Phys. Rev. Lett. **101**, 077005 (2008).
[11] A. J. Drew *et al*., Nature Mater. **8**, 310 (2009).
[12] F. Han, B. Shen, Z. Y. Wang, and H. H. Wen, arXiv:1103.1347.
[13] C. C. Homes, Z. J. Xu, J. S. Wen, and G. D. Gu, arXiv:1110.5529.
[14] B. Shen, B. Zeng, G. F. Chen, J. B. He, D. M. Wang, H. Yang, and H. H. Wen, Europhys. Lett. **96**, 37010 (2011).
[15] M. I. Tsindlekht, I. Felner, M. Zhang, A. F. Wang, and X. H. Chen, Phys. Rev. B **84**, 052503 (2011).
[16] A. Ricci *et al*., Supercond. Sci. Technol. **24**, 082002 (2011).
[17] R. H. Yuan, T. Dong, Y. J. Song, P. Zheng, G. F. Chen, J. P. Hu, J. Q. Li, and N. L. Wang, Sci. Rep. **2**, 221 (2012).
[18] R. W. Hu *et al*., arXiv:1201.0953.
[19] Y. J. Uemura *et al*., Phys. Rev. Lett. **62**, 2317 (1989).
[20] C. Bernhard, J. L. Tallon, T. Blasius, A. Golnik, and C. Niedermayer, Phys. Rev. Lett. **86**, 1614 (2001).
[21] J. J. Ying, Z. J. Xiang, Z. Y. Li, Y. J. Yan, M. Zhang, A. F. Wang, X. G. Luo, and X. H. Chen, Phys. Rev. B **85**, 054506 (2012).
[22] A. Schenck, *Muon Spin Rotation Spectroscopy: Principles and Applications in Solid State Physics* 1 ed. (Taylor & Francis, Bristol, 1985).
[23] H. Maeter *et al*., Phys. Rev. B **80**, 094524 (2009).
[24] C. Bernhard, J. Humlícek, and B. Keimer, Thin Solid Films **455–456**, 143 (2004).
[25] K. W. Kim, M. Rössle, A. Dubroka, V. K. Malik, T. Wolf, and C. Bernhard, Phys. Rev. B **81**, 214508 (2010).
[26] A. B. Kuzmenko, Rev. Sci. Instrum. **76**, 9 (2005).
[27] Z. Shermadini *et al*., Phys. Rev. Lett. **106**, 117602 (2011).
[28] Z. Shermadini, H. Luetkens, R. Khasanov, A. Krzton-Maziopa, K. Conder, E. Pomjakushina, H.-H. Klauss, and A. Amato, Phys. Rev. B **85**, 100501(R) (2012).
[29] A. J. Drew *et al*., Phys. Rev. Lett. **101**, 097010 (2008).
[30] P. Marsik *et al*., Phys. Rev. Lett. **105**, 057001 (2010).
[31] H. Luetkens *et al*., Nat. Mater. **8**, 305 (2009).
[32] C. Bernhard *et al*., Phys. Rev. B **52**, 10488 (1995).
[33] A. Charnukha, J. Deisenhofer, D. Pröpper, M. Schmidt, Z. Wang, Y. Goncharov, A. N. Yaresko, V. Tsurkan, B. Keimer, A. Loidl, and A. V. Boris, Phys. Rev. B **85**, 100504(R) (2012).
[34] A. Dubroka *et al*., Phys. Rev. Lett. **106**, 047006 (2011).
[35] C. C. Homes, A. Akrap, J. S. Wen, Z. J. Xu, Z. W. Lin, Q. Li, and G. D. Gu, J. Phys. Chem. Solids **72**, 505 (2011).
[36] A. Sihvola, *Electromagnetic Mixing Formulas and Applications* (Institution of Electrical Engineers, Stevenage, Hertfordshire, UK, 1999).
[37] S. C. Speller, T. B. Britton, G. M. Hughes, A. Krzton-Maziopa, E. Pomjakushina, K. Conder, A. T. Boothroyd, and C. R. M. Grovenor, arXiv:1204.5472.
[38] T. G. Mayerhöfer, Z. Shen, R. Keding, and J. L. Musfeldt, Phys. Rev. B **71**, 184116 (2005).
[39] E. Shiles, T. Sasaki, M. Inokuti, and D. Y. Smith, Phys. Rev. B **22**, 1612 (1980).
[40] E. van Heumen, Y. Huang, S. de Jong, A. B. Kuzmenko, M. S. Golden, and D. van der Marel, Europhys. Lett. **90**, 37005 (2010).
[41] N. Barišić, D. Wu, M. Dressel, L. J. Li, G. H. Cao, and Z. A. Xu, Phys. Rev. B **82**, 054518 (2010).
[42] D. Wu *et al*., Phys. Rev. B **81**, 100512 (2010).
[43] J. N. Hancock, S. I. Mirzaei, J. Gillett, S. E. Sebastian, J. Teyssier, R. Viennois, E. Giannini, and D. van der Marel, Phys. Rev. B **82**, 014523 (2010).
[44] C. C. Homes, A. Akrap, J. S. Wen, Z. J. Xu, Z. W. Lin, Q. Li, and G. D. Gu, Phys. Rev. B **81**, 180508 (2010).
[45] P. Cai, C. Ye, W. Ruan, X. D. Zhou, A. F. Wang, M. Zhang, X. H. Chen, and Y. Y. Wang, Phys. Rev. B **85**, 094512 (2012).
[46] W. Li *et al*., Nat. Phys. **8**, 5 (2012).
[47] S. Tajima, T. Kakeshita, Y. Fudamoto, N. L. Wang, V. Železný, K. M. Kojima, S. Uchida, B. Gorshunov, and M. Dressel, J. Phys. Chem. Solids **67**, 321 (2006).
[48] T. Qian *et al*., Phys. Rev. Lett. **106**, 187001 (2011).
[49] X. P. Wang, T. Qian, P. Richard, P. Zhang, J. Dong, H. D. Wang, C. H. Dong, M. H. Fang, and H. Ding, Europhys. Lett. **93**, 57001 (2011).
[50] Y. Zhang *et al*., Nat. Mater. **10**, 273 (2011).